6-15-2018

Reaction Mechanism for Oxygen Evolution on RuO2, IrO2, and RuO2@IrO2 Core-Shell Nanocatalysts

Julie N. Renner
Case Western Reserve University, julie.renner@case.edu

Author(s) ORCID Identifier:

Julie N. Renner

Recommended Citation

Ma, Z., Zhang, Y., Liu, S., Xu, W., Wu, L., Hsieh, Y. C., Liu, P., Zhu, Y., Sasaki, K., Renner, J.N., Ayers, K.E., Adzic, R.R., & Wang, J. X. Reaction mechanism for oxygen evolution on RuO2, IrO2, and RuO2@ IrO2 core-shell nanocatalysts. Journal of Electroanalytical Chemistry, 2018, 819, 296-305.

BNL-114508-2017-JAAM

Reaction mechanism for oxygen evolution on RuO2, IrO2, and RuO2@IrO2 core-shell nanocatalysts

Z. Ma, J. X. Wang

To be published in "Journal of Electroanalytical Chemistry"

November 2017

Chemistry Department

Brookhaven National Laboratory

U.S. Department of Energy

USDOE Office of Science (SC),

USDOE Office of Science (SC), Basic Energy Sciences (BES) (SC-22)

DISCLAIMER

BNL-114508-2017-JA

Reaction mechanism for oxygen evolution on RuO2, IrO2, and RuO2@IrO2 core-shell nanocatalysts

D. V. Matyushov

Submitted to Journal of Electroanalytical Chemistry

November 2017

Chemistry Department

Brookhaven National Laboratory

U.S. Department of Energy
[DOE Office of Science]

DISCLAIMER

Reaction mechanism for oxygen evolution on RuO_2, IrO_2, and RuO_2@IrO_2 core-shell nanocatalysts

Zhong Ma[a] , Yu Zhang[a], Shizhong Liu[a], Wenqian Xu[b], Lijun Wu[a], Yu-Chi Hsieh[a]
Ping Liu[a], Yimei Zhu[a], Kotaro Sasaki[a], Julie N. Renner[c],
Katherine E. Ayers[c], Radoslav R. Adzic [a,*], and Jia X. Wang [a,*]

[a]*Brookhaven National Laboratory, Chemistry Division, Energy & Photon Sciences Directorate, Upton, NY 11973, USA*

[b]*X-ray Science Division, Advanced Photon Source, Argonne National Laboratory, Argonne, IL 60439, USA*

[c]*Proton OnSite, 10 Technology Drive, Wallingford, CT 06492, USA*

In memoriam of Professor Roger Parsons

Abstract

Iridium dioxide, IrO_2, is second to the most active RuO_2 catalyst for the oxygen evolution reaction (OER) in acid, and is used in proton exchange membrane water electrolyzers due to its high durability. To improve the activity of IrO_2-based catalysts, we prepared RuO_2@IrO_2 core-shell nanocatalysts using carbon-supported Ru as the template. At 1.48 V, the OER specific activity of RuO_2@IrO_2 is threefold that of IrO_2. While the activity volcano plots over wide range of materials have been reported, zooming into the top region to clarify the rate limiting steps of most active catalysts is important for further activity enhancement. Here, we verified theory-proposed sequential water dissociation pathway in which the O-O bond forms on a single metal site, not via coupling of two adsorbed intermediates, by fitting measured polarization curves using a kinetic equation with the free energies of adsorption and activation as the parameters. Consistent with theoretical calculations, we show that the OER activities of IrO_2 and RuO_2@IrO_2 are limited by the formation of O adsorbed phase, while the OOH formation on the adsorbed O limits the reaction rate on RuO_2.

KEYWORDS: Electrolysis; RuO_2; IrO_2; Core-shell; Oxygen evolution reaction mechanism.

Corresponding Authors *E-mail addresses: jia@bnl.gov (JX Wang) adzic@bnl.gov (RR Adzic)

1. Introduction

The core-shell nanoparticles were widely studied over the past decade for various applications in catalysis, energy storage, sensors, and in biology [1]. With the advanced technologies for their synthesis and structural characterization, an atomic level control of core-shell structures were achieved for Pt shells on other metals or metal-alloys cores [2–4]. Utilizing 1- to 2-monolayer-thick Pt shells maximizes the surface area per Pt mass, and enables fine tuning of the surface properties with suitable core metals and Pt shell thicknesses. Coupled with progress in density functional theory (DFT) calculations [5], the rational design of core-shell nanocatalysts became a practical approach. For example, Pd and Co- or Ni-containing alloys are suitable cores [2,6,7] for oxygen reduction reaction (ORR) [2,6,7], and well-ordered Ru@Pt core-shell nanocatalysts are more active than are Pt nanoparticles for hydrogen oxidation reaction (HOR) and hydrogen evolution reaction (HER) [8], especially in alkaline environments [9]. The enhancements in specific activities of these metallic core-shell particles are ascribed to optimized binding energies for the adsorbed reaction intermediates, O and OH for the ORR [2,6] and H for the HOR-HER [9,10].

Like Pt, Ir is expensive and is even rarer than is Pt in the Earth's crust [11]. Thus, considerable research efforts were made to lower the IrO_2 loading without compromising the OER performance [12–14]. A threefold enhancement in Ir mass activity was reported for the IrNi@IrOx catalysts, which have a metal@metal-oxide hybrid core@shell architecture, prepared by surface oxidation of the IrNi alloy nanoparticles, the surface of which were Ir-enriched by electrochemical de-alloying Ni [15]. Since non-noble metals are prone to dissolution in acid, Ru, a significantly cheaper noble metal, was a common choice in developing mixed oxide nanocatalysts for the OER in PEM water-electrolyzers [16–22]. RuO_2 is known to be the most active for the OER in acids [23,24], but not sufficiently durable, and thus, Ru-Ir mixed oxides were studied for enhancing the OER activity and catalysts' durability. Recently, the stability of $Ru_{0.5}Ir_{0.5}O_2$ catalyst was found to be four times higher after treatment to enrich Ir at its surface [25]. In this study, we prepared RuO_2@IrO_2 core-shell nanocatalysts, which exhibit a threefold enhancement in specific activity at 1.48 V compared to IrO_2.

Several OER mechanisms have been proposed for metal dioxides in acids, which can be categorized by whether it involves a reaction that combines two adsorbed oxygen species (either OH, or O, or OOH) at neighboring sites [26]. The coupling pathway with the O-O bond formation via a non-electron-transfer reaction of two surface species was preferred in early studies[27–31] because the observed potential- and catalyst-dependent Tafel slopes were qualitatively interpreted by having a reaction step with its rate independent of potential. Later in the 2000s, however, DFT studies suggested sequential water dissociation as the favorable pathway, in which the O-O bond forms at a single surface site by adding the second O to a previously adsorbed O [32–36]. Taking RuO_2 as an example, the DFT calculated reaction barrier for the coupling pathway has been found higher than that for the sequential pathway [37]. This distinctly differs from that hydrogen evolution reaction on Pt, where the Volmer-Tafel pathway in which two adsorbed H species combine to form H_2 is dominant. In this study, following the theoretic insight, we derived a kinetic equation based on a sequential pathway to fit measured OER polarization curves over a wide potential region using adsorption and activation free energies as the adjustable parameters. The non-linear polarization curves in the Tafel plot for RuO_2, IrO_2, and RuO_2@IrO_2 were well reproduced by the best fits. The results demonstrated that small and gradual changes in Tafel slopes are not necessarily caused by a coupling pathway involving O-O bond formation via two adsorbed intermediates. In addition, we present DFT-calculated results in Theoretical section, which provide insight on the effect of O adsorption energy on the rate-limiting steps and the OER activity trend.

2. Materials and methods

2.1. Preparation of RuO_2 and RuO_2@IrO_2 nanocatalysts

In a typical synthesis of a RuO_2 nanocatalyst, commercial carbon-supported Ru metal nanoparticles (40 wt% Ru/C, E-Tek) were calcined in air at 400 °C for 1 h using a tube furnace. An antistatic gun (Zerostat, SPI Supplies) was used to neutralize static charges whilst transferring the sample. For preparing RuO_2@IrO_2 nanocatalysts, hydrogen hexachloroiridate(IV) hexahydrate (H_2IrCl_6-$6H_2O$, 40% Ir, Acros Organics) was dissolved in anhydrous ethanol (200 proof, ACS/USP Grade, Pharmco Aaper). The ethanolic H_2IrCl_6 solution was heated in an oil bath at 80 °C for 1 h until the solution color changed from brown to light yellow. Then, carbon-supported Ru metal nanoparticles (20 wt% Ru/C, E-Tek) were added into

the solution at 40 °C with stirring, and the solvent was evaporated by heating the mixture in an oil bath at 85 °C. The dry mixture was crushed into fine powder, and calcined in air at 400 °C for 1 h in a tube furnace.

2.2. *Structural characterization of the metal oxide nanocatalysts*

Transmission electron microscope (TEM), scanning transmission electron microscopy (STEM) imaging and electron energy-loss spectroscopy (EELS) were carried out using the double aberration-corrected JEM-ARM200CF microscope with a cold-field emission gun and operated at 200 kV. The microscope is equipped with JEOL and Gatan HAADF detectors for incoherent STEM-HAADF (Z-contrast) imaging, Gatan GIF Quantum ER Energy Filter with dualEELS for EELS. Powder X-ray diffraction (PXRD) measurements were carried out on Beamline 17-BM (λ = 0.75009 Å) of the Advanced Photon Source at Argonne National Laboratory. Sample powder was packed in 0.5 mm inner diameter Kapton® capillaries and measured in transmission geometry with PerkinElmer® amorphous Si flat panel detector.

2.3. *Preparation of gas diffusion electrodes*

The catalyst inks were prepared by dispersing metal oxide nanoparticles in a solution of deionized water, iso-propanol, and Nafion® (perfluorinated resin, equivalent weight 1000, Aldrich). Typically, the dry mass of Nafion® is equal to 5% of the weight of the catalyst. The volume ratio for water to iso-propanol was 3:1. We used a Mixer Mill MM 400 (Retsch) to shake the mixture at a frequency of 12 s^{-1} for 1 hour, and sonicated it in an ice bath for 5 - 10 min before each use. Inks of 10 to 40 μL were pipetted on to 1 cm^2 area at one end of a 1×4 cm^2 strip of a Ti-based gas diffusion layer (from Proton OnSite) to obtain the desired catalyst loadings.

2.4. *Electrochemical measurements*

All electrochemical measurements were performed with a three-electrode cell using a Volta PGZ402 potentiostat (Voltalab, Radiometer Analytical) at room temperature. The Ti gas diffusion electrode strips were held vertically with the catalyzed part (1×1 cm^2) immersed in 0.5 M H_2SO_4 solution facing a Pt flag counter electrode at a distance of 1 – 2 cm. Potentials were measured using a leak-free (Ag/AgCl, 3M NaCl) reference electrode, and converted to the

reversible hydrogen electrode (RHE) scale using measured open-circuit potential of the Pt flag in the H_2-saturated electrolyte. Chronopotentiometry at 200 mA cm^{-2} was carried out for 1 h to eliminate the samples having easy-to-fall-off catalysts under oxygen bubbling condition. It was followed by measurement of electrochemical impedance at 1.8 V versus RHE with a peak-to-peak perturbation of 20 mV with an AC frequency from 10 kHz to 0.1 Hz to determine the high frequency resistance (HFR) that is typically about 1 Ω cm^2. The ohmic-loss corrected potential, *E-iR*, denotes applied potential *E* minus the product of measured current *i* and *HFR*. Quasi-static polarization curves were obtained by averaging the currents measured during a positive and a negative potential sweep at 20 mV s^{-1}. The integrated charge from 0.4 to 1.23 V in a voltammetry curve was obtained by averaging the two values obtained from positive and negative sweeps.

2.5. *Computational method*

Spin-polarized DFT calculations were performed using the CASTEP code.[38,39] The generalized gradient approximation (GGA) [40] with the Perdew–Burke–Ernzerhof functional (RBE) [41] was used to describe the exchange and correlation potential. The cutoff energy for the plane-wave basis set was set at 380 eV in all calculations. The Monkhorst-Pack [42] mesh k-points ($4 \times 4 \times 1$) were used for the slab calculations. To model the rutile IrO_2(110), RuO_2(110), and TiO_2(110) surfaces, four O-Ru(Ir,Ti)-O trilayers with a (2×2) array in each layer were used, wherein the bottom two trilayers were fixed at the bulk position and the rest of the atoms were allowed to relax with the adsorbates. This setup is the same as used in the previous DFT calculations for the OER on metal oxides [33]. For the RuO_2@IrO_2 and TiO_2@IrO_2 catalysts, Ru and Ti, respectively, were replaced by Ir in the top layer of the oxide models. A vacuum gap of 15 Å in the z-direction was introduced to separate two subsequent slabs. The free energies for each reaction intermediate involved in the OER, $\Delta G = \Delta E + \Delta ZPE - T\Delta S$, were calculated based on the method reported previously [32]. It involves setting the reference potential to be that of the standard hydrogen electrode so that the chemical potential (the free energy per H) for ($H^+ + e^-$) in solution can be related to that of ½ H_2 in gas phase. The entropies and zero point energies were from those given in the reference [32].

3. Theoretical Calculation

We employed DFT to calculate the free energies for the stable reaction intermediates involved in the OER on the rutile (110) metal dioxide surfaces (Fig. 1a), including RuO_2(110), IrO_2(110), and IrO_2 monolayer on RuO_2(110) and TiO_2(110). TiO_2 itself is rather inactive for the OER, but it is stable in acid. In addition, TiO_2 has larger, while RuO_2 has smaller, lattice constants than IrO_2 does. So the effects of these two oxide cores can show whether a lattice-mismatch-induced surface expansion or contraction is more beneficial in promoting the OER activity on the IrO_2 surface. Similar to Pt(111) being used to represent polycrystalline Pt and Pt nanoparticles in DFT calculations, we chose rutile (110) surface, like previous DFT studies [33,34,37], because it is the most stable facet of these dioxides. This approximation was made for studying material effect in the activity trend, and thus, our comparisons with experimentally derived free energies for nanocatalysts with multiple facets were not meant for absolute values, but for linear correlation in trend among the catalysts of different metal oxides on the surface and in the core.

The most stable adsorbates for each of the nominal metal oxidation states from 3 to 7 are identified as shown in Fig. 1b. In the short notations, the asterisk indicates the following species having a bond with the surface. Since the nominal oxidation state is the hypothetical charge for a surface metal atom assuming all bonds with different elements were 100% ionic, it is +4 for bare MO_2 and varies by adding 2 for each O atom and subtracting 1 for each H atom in the adsorbed species. Thus, proton desorption is oxidative as it leads to higher oxidation states, while water dissociative adsorption does not affect the nominal oxidation state because the effect of adding two H cancels out that of adding one O.

Using bare oxide surfaces and free water molecules as the zero energy references, the reaction free energies for forming these adsorbed phases at E = 0 V versus RHE are shown in Fig. 1c. The dotted lines leading to the *OH*H phase are all downward indicating that water dissociation is exothermic on the three oxides, which result in a *OH on the coordinately unsaturated metal site (cus), M_{cus} and an *H on the bridge oxygen, O_{br} (Fig. 1a). With a similar free energy as the *OH*H phase does, the *H phase is expected to co-exist with the *OH*H below the oxygen reversible potential of 1.23 V. In simplification, earlier DFT study termed the surface being OH covered at potentials below the OER region [33].

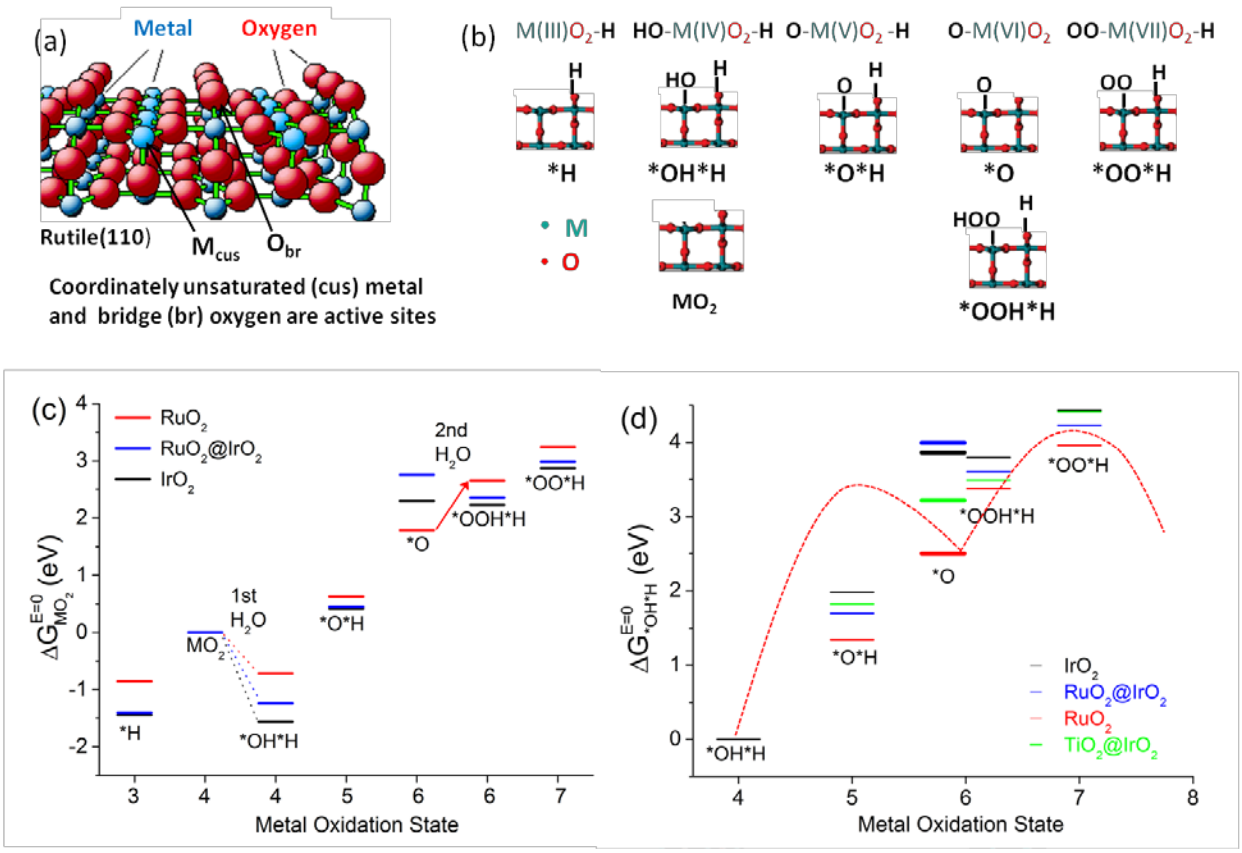

Figure 1. (a) Atomic model of a rutile (110) metal dioxide surface. (b) Energetically favorable adsorbates from water dissociation and the OER in acid for each of the metal oxidation states from 3 to 7. (c,d) DFT-calculated reaction free energies at E = 0 V vs. RHE with energy zero referenced to an adsorbates-free oxide surface labeled as MO_2 in (c) and referenced to the *OH*H phase in (d). The red dotted curves in (d) schematically illustrate a kinetic model with two major steps for the OER on RuO_2.

For the OER at high potentials, oxidative deprotonation occurs preferably from the *OH group forming the *O*H phase, and then, from the *H on the O_{br} site forming the *O phases. With the O_{br} site freed by *H desorption, the second water dissociation can occur on the *O phase, forming *OOH on the M_{cus} and *H on the O_{br} sites. This reaction is endothermic on RuO_2 (upward red arrow), while it remains exothermic for the RuO_2@IrO_2 and IrO_2. Before O_2 evolution, a proton firstly desorbs from the *OOH group to form the *OO*H phase. For RuO_2@IrO_2 and IrO_2, the exothermic water dissociation on O adsorbed metal site results in a facile formation of the O-O bond on single metal site, and thus, clearly supports the sequential pathway. The endothermic water dissociation on O-adsorbed RuO_2 questions on whether forming the O-O bond via coupling two *O could have lower activation barrier. As found by a

previous DFT study, the barrier is higher for coupling two adsorbed O than for the sequential pathway on RuO_2 [37].

To describe the OER kinetics, we plotted the reaction free energies in Fig. 1d using the *OH*H phase to set energy zero reference because this is the dominant phase at the oxygen reversible potential with the lowest energy state. The *O phase plays a central role as it is the precursor for the O-O bond formation. As shown by the thick bars, the reaction free energies for the *O phase, which are higher in the order of RuO_2 (2.50 eV) < TiO_2@IrO_2 (3.22 eV) < IrO_2 (3.86 eV) < RuO_2@IrO_2 (4.00 eV), indicating a weakening of O adsorption. The particularly strong O adsorption on RuO_2 results from a large structural distortion of the more flexible RuO_2 surface as compared to other surfaces. Compared to bulk IrO_2, the O adsorption on the IrO_2 monolayer is weakened by a RuO_2 substrate, while it is strengthened by TiO_2. These effects are understandable based on lattice-mismatch-induced contraction and expansion. Relative to the two in-plane lattice constants for Ir-O and Ir-Ir, those for Ru-O and Ru-Ru are smaller by -0.44% and -0.67%, respectively, and larger by 1.86% for Ti-O and 0.38% for Ti-Ti.[43] The results provide a case of lattice-mismatch effects on adsorption energies for oxides, similar to the well-known cases for metal surfaces, which were utilized for enhancing the activities of fuel cell catalysts for HOR [9] and ORR [44,45].

In identifying the rate-limiting step and predicting the relative activities of the four oxide surfaces, we calculated the energy gaps for the reactions leading to the nominal oxidation state of 5, 6, and 7, i.e., the *O*H phase, the *O or *OOH*H phase (whichever is lower in energy), and the *OO*H phase. Choosing the lower of the two, rather than always taking the free energy for *O and ignoring that for *OOH*H, appears more reasonable because the intermediate with lower energy should have higher coverage, and thus, plays a more important role in determining reaction kinetics. The largest energy gaps among the three reactions for each of the catalysts are 1.46 (*OO*H, RuO_2) < 1.83 (*O*H, TiO_2@IrO_2) < 1.91 (*OOH*H, RuO_2@IrO_2) < 1.98 (*O*H, IrO_2) eV. The higher is a barrier for the rate-limiting step, the lower OER activity of the catalyst. Thus, the DFT calculations found the OER activity decreasing in the order of RuO_2 > TiO_2@IrO_2 > RuO_2@IrO_2 > IrO_2. All three IrO_2-based catalysts have the rate-limiting step in either the first or second deprotonation process toward the formation of the *O phase, while the

reaction rate on RuO_2 is limited by the formation of *OO*H that involves an endothermic water dissociation on the *O phase in forming the O-O bond followed by deprotonation.

Detailed in Section 5, the theoretical results on the activity trend and rate-limiting steps are consistent with the conclusions based on kinetic analysis of measured polarization curves using a simplified kinetic model that involves *O as the single reaction intermediate and two major reaction steps. As schematically illustrated by the red dotted curves in Fig. 1d, using RuO_2 as an example, the first step leads to the formation of *O phase and the second step results in its removal via O_2 formation and desorption from the catalysts' surface.

4. Results

4.1. *Catalyst synthesis and structural characterization*

Figure 2 shows the synthesis methods, X-ray diffraction profiles, and the TEM images for the RuO_2 and RuO_2@IrO_2 (Ir:Ru atomic ratio 1.17:1.0 or 0.54:0.46) nanocatalysts we prepared in comparison with those for the commercial IrO_2 nanocatalyst used in PEM water electrolyzers. The Adams fusion method used in commercial production of unsupported IrO_2 catalyst involves mixing the H_2IrCl_6 precursor with $NaNO_3$, heating the dried mixture in air at 350 - 500 °C for 0.5 - 2 h, and washing off remaining salts ($NaNO_3$ and NaCl) [46,47]. The produced IrO_2 catalysts usually contain aggregates of small, amorphous IrO_2 nanoparticles as shown by the TEM image in Fig. 2e. A few large metallic Ir particles may coexist as indicated by the sharp XRD spikes (black line in Fig. 2b). We take this IrO_2 sample as the baseline reference for performance comparison because the catalyst is industrial standard for PEM water electrolyzers and it exhibits the typical characteristics of IrO_2 in voltammetry and polarization measurements [23,48].

We prepared RuO_2 and RuO_2@IrO_2 nanocatalysts using well-dispersed Ru nanoparticles on a carbon support (Ru/C) as the precursor of RuO_2, and using H_2IrCl_6 as the precursor of IrO_2 shell (Fig. 2a). The carbon support as a template in the Ru/C (20 or 40 wt%) was burnt off during calcinations at temperatures between 350 and 450 °C in air, yielding unsupported metal dioxide nanoparticles as ready-to-use OER catalysts. In Table S1, we list the weights of samples made with different Ru/C ratios and at different calcining temperatures. All but one that was made with 10 wt% Ru/C weigh as expected for unsupported metal dioxides (within 5% of the values

calculated from the amount of metals in the precursors). It appears that Ru nanoparticles catalyze carbon combustion, and thus, a higher Ru weight percentage on a carbon support facilitates the complete elimination of carbon. The catalytic effect of Ru in removing carbon is supported by the findings in a study of preparing Pt-RuO_2/C catalysts [49], in which the weight loss from a Pt-RuO_2/C sample started around 350 °C while the carbon-only sample showed a weight loss above 500 °C.

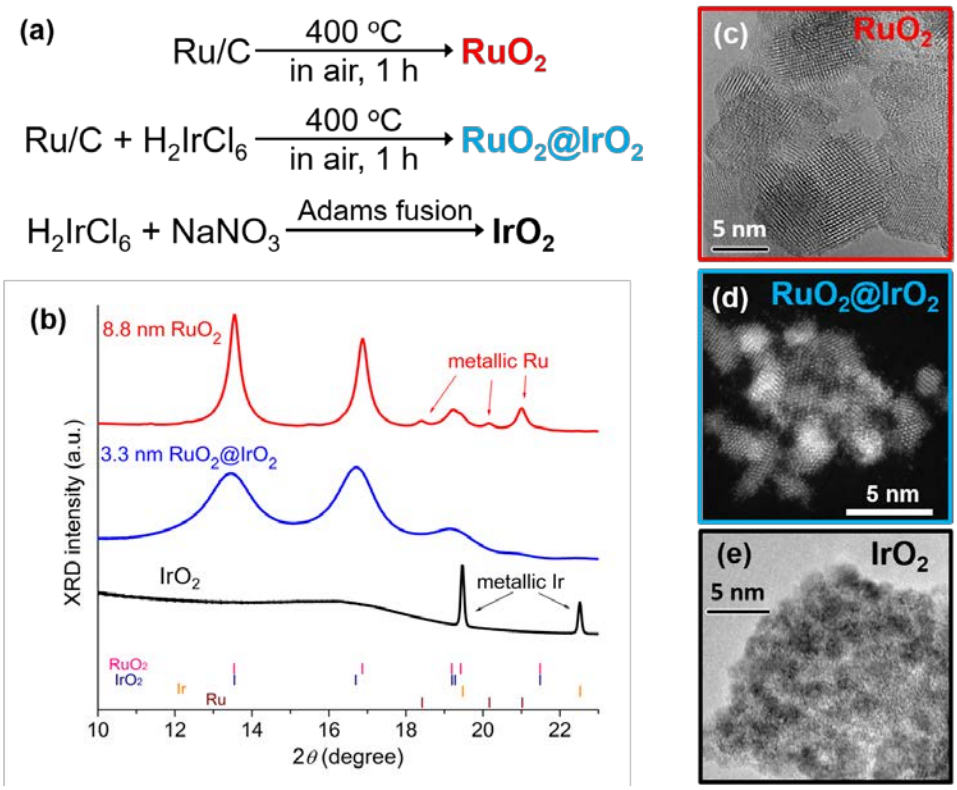

Figure 2. (a) Synthetic schemes. (b) Synchrotron XRD profiles of the RuO_2 (red), RuO_2@IrO_2 (blue), and IrO_2 (black) catalysts with the reference peak positions marked by the bars. λ = 0.75009 Å. Particle sizes are determined using the Scherrer equation. (c) TEM image of RuO_2. (d) STEM image of RuO_2@IrO_2 particles. (e) TEM image of a commercial IrO_2 catalyst.

The synchrotron XRD profiles for a RuO_2 sample made with 40 wt% Ru/C and a RuO_2@IrO_2 sample made using 20 wt% Ru/C with H_2IrCl_6 (Fig. 2b) exhibit the major XRD peaks at the positions for RuO_2 and IrO_2 rutile structures (space group $P4_2/mnm$). The average sizes of the particles are 8.8 and 3.3 nm, respectively, consistent with the TEM images shown in Figs. 1c and 1d. They differ, partly due to the larger Ru particles in the 40 wt% than those in the 20 wt% Ru/C used as the starting materials, and partly because Ir diffuses more slowly than Ru

does, which likely facilitated the formation of smaller RuO_2@IrO_2 particles. Suggested by the weak XRD peaks at the metallic Ru positions for the 8.8 nm RuO_2 particles, the inner core of the Ru particles may not be as fully oxidized as the 3.3 nm RuO_2@IrO_2 particles. With an Ir/Ru atomic ratio of 1.17/1, the thickness of IrO_2 is close to one monolayer for 3.3 nm particles when the distribution is uniform. Quantifying the degree of core-shell structure was difficult because rather weak intensity contrast was expected in STEM-HAADF and EELS measurements to distinguish a monolayer shell on small nanoparticles. Indirectly, we show, in the next section, that the RuO_2@IrO_2 sample exhibited distinct voltammetry feature suggesting the core-shell nanoparticles being dominant.

4.2. *Voltammetry curves and oxide surface area*

The typical voltammetry curves for the RuO_2, RuO_2@IrO_2, and IrO_2 nanocatalysts in acid are shown in Fig. 3a with the current normalized to the oxide surface area. The rather high, near constant currents between 0.4 and 1.23 V distinctly differ from the voltammetry curves on Pt and Au metal surfaces, in which a low current region is free of chemically adsorbed species. This is because water dissociation is exotic on the oxide surfaces, while H and OH adsorption on noble metals occurs only at sufficiently low and high potentials, respectively. Using IrO_2 as an example, we show schematically in Fig. 3b that the dissociative water adsorption leads to an OH and H co-adsorbed phase (HO-IrO_2-H) that likely dominates near 1.23 V; lowering the potential causes a gradual loss of the OH from the unsaturated metal sites, M_{cus}, while the bridge oxygen sites, O_{br}, remain covered by H (Fig. 1a). This simplified surface phase diagram is based on the comparable free energies for the *H and *OH*H phases at low potentials and the general trend of higher coverage of more oxygenated phase at higher potentials. Recently, a Pourbaix diagram for the IrO_2 (110) surface was constructed theoretically using machine learning to handle a large number of possible adsorption configurations [50]. The essential feature presented in the abstract is that the *H phase is the most stable at low potentials, followed by a *OH and *H mixed phase, and then the *OH phase with increasing potential. That is consistent with our estimated phase diagram presented in terms of coverage at the potentials below the potential for the *OH dominant phase. Below 0.4 V, the voltammetry behavior is not well understood. For RuO_2, an experimental study suggested the formation of Ru(II) phase at 0.4 V [51]. However, the surface phase diagram constructed from DFT calculations only confirmed the phases with Ru oxidation

state above (III) [52]. We exclude the region below 0.4 V in the following comparison of the catalysts.

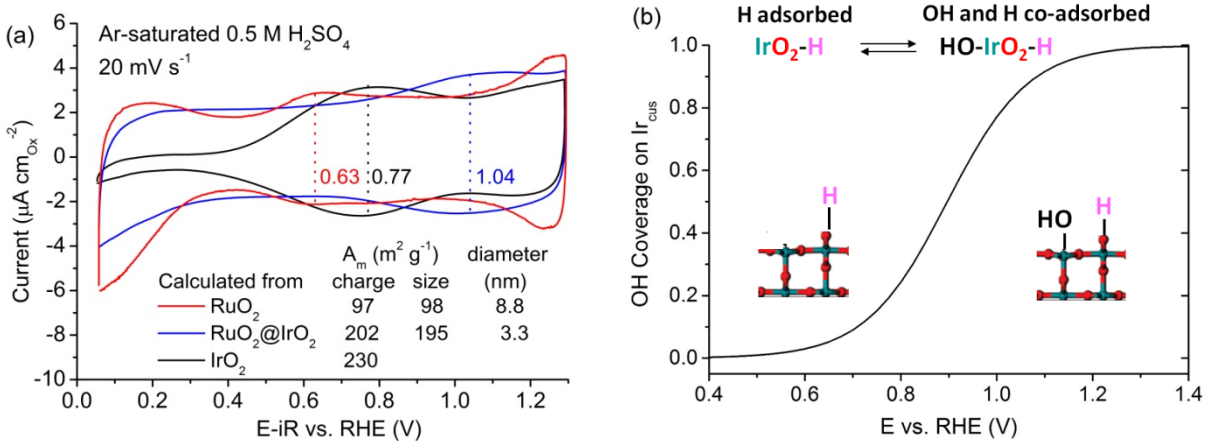

Figure 3. (a) Voltammetry curves with current normalized to the oxide surface areas estimated from the charge integrated between 0.4 and 1.23 V, which was obtained by averaging the absolute charges in the positive and negative potential sweeps. The specific areas (A_m) calculated from charge-deduced area and particle-size-dependent area are given with the average diameter of the nanoparticles. The metal oxide loadings were the same as those given in Fig. 4a. (b) Schematic illustration of the reversible Ir(III)/Ir(IV) redox reaction on the IrO_2 rutile (110) surface in acid, which involves OH adsorption/desorption on the Ir surface sites while H adsorbs on the bridge O site over the whole potential region. Green dots are Ir and red dots are oxygen in the IrO_2 surface model.

A catalyst-specific voltammetry feature is the potential for a pair of broad, nearly reversible current peaks as marked by the dotted vertical lines in Fig. 3a, which increases in the order of RuO_2 (0.63 V) < IrO_2 (0.77 V) < RuO_2@IrO_2 (1.04 V), indicating the surface phase transition from *H to *OH*H or metal surface oxidation from (III) to (IV) is increasingly more difficult in that order. The fact that the RuO_2@IrO_2 is not in the middle between RuO_2 and IrO_2 signifies a surface property of core-shell nanoparticles because one cannot generate such a feature by mixing RuO_2 and IrO_2 particles. In addition, near the high potential limit at 1.23 V, the current rises most on RuO_2, signaling the onset of *OH phase formation on RuO_2. The absence of this feature for the RuO_2@IrO_2 sample indicates that majority RuO_2 cores were covered by IrO_2 shells. In contrast, the voltammetry curve for Ru-Ir mixed oxide is similar to the average of the curves for RuO_2 and IrO_2 [53].

For estimation of mass-normalized oxide surface area, A_m, we used two methods. The results are consistent as given in Fig. 3a. One method estimates the surface area from the

integrated charges of the voltammetry curves between 0.4 and 1.23 V, using a charge density of 0.10 mC cm^{-2}. This value is based on the atomic density of the surface metal atoms and the assumption of a 1e/metal-atom redox reaction. The values for the rutile (110) and (100) facets are listed in Table S2. For nanoparticles with both facets, the averaged charges for 1e/metal-atom redox were about the same 0.10 mC cm^{-2} for IrO_2 and RuO_2. This value is about half of the commonly used charge density of 0.21 mC cm^{-2} for polycrystalline Pt because metallic Pt has a facet-averaged atomic density about twice of those for IrO_2 and RuO_2 (Table S3). Based on the same 1e/metal-atom assumption, a study using the (110) and (100) surfaces of rutile RuO_2 and IrO_2 showed that the atomic densities estimated from the charges integrated between 0.3 to 1.25 V are higher by 12% to 21% than the values calculated from the lattice constants [48]. Better agreements would be obtained using a smaller potential range, supporting the choice of potential range from 0.4 and 1.23 V.

Independent of voltammetry measurements, we estimated the surface area per oxide mass based on the particle-size-dependent geometric areas using A_m = area / (volume × density) = 6 / ($d \times \rho$) where d is the diameter of the spherical particles and ρ *i*s the density of the dioxides (detailed in Table S4). The values for the RuO_2 and RuO_2@IrO_2 samples are consistent with those obtained from measured charges as listed in Fig. 3a.

4.3. *Steady-state OER polarization and oxide-mass activities*

In the OER polarization measurements, we used high oxide loadings (~1 mg cm^{-2}) on Ti gas diffusion electrodes and strong acidic electrolyte (0.5 M H_2SO_4) to be close to the high- current conditions in PEM water electrolyzers. Figure 4 shows the results using 1 cm^2 electrode surface area with the OER currents up to 400 mA. Oxygen bubbling at high currents sometimes knocks off catalyst particles causing a sudden change of measured current or voltage. To obtain reliable steady-state polarization curves, we first ran 1 h chrono-potentiometry at 200 mA cm^{-2} to ensure at least the particles survived were well attached on the electrode in the following measurements. Figure 4a shows the voltages measured for the three catalysts were all stabilized near the end of 1 h. After impedance measurement that determined the high frequency resistance (HFR), the OER polarization curves were obtained by averaging the currents in the positive and negative potential sweeps (Fig. 4b), and correcting the uncompensated ohmic loss in potential using the

measured HFR. Averaged currents represent the steady-state reaction rates when coverage of the intermediates reaches equilibrium.

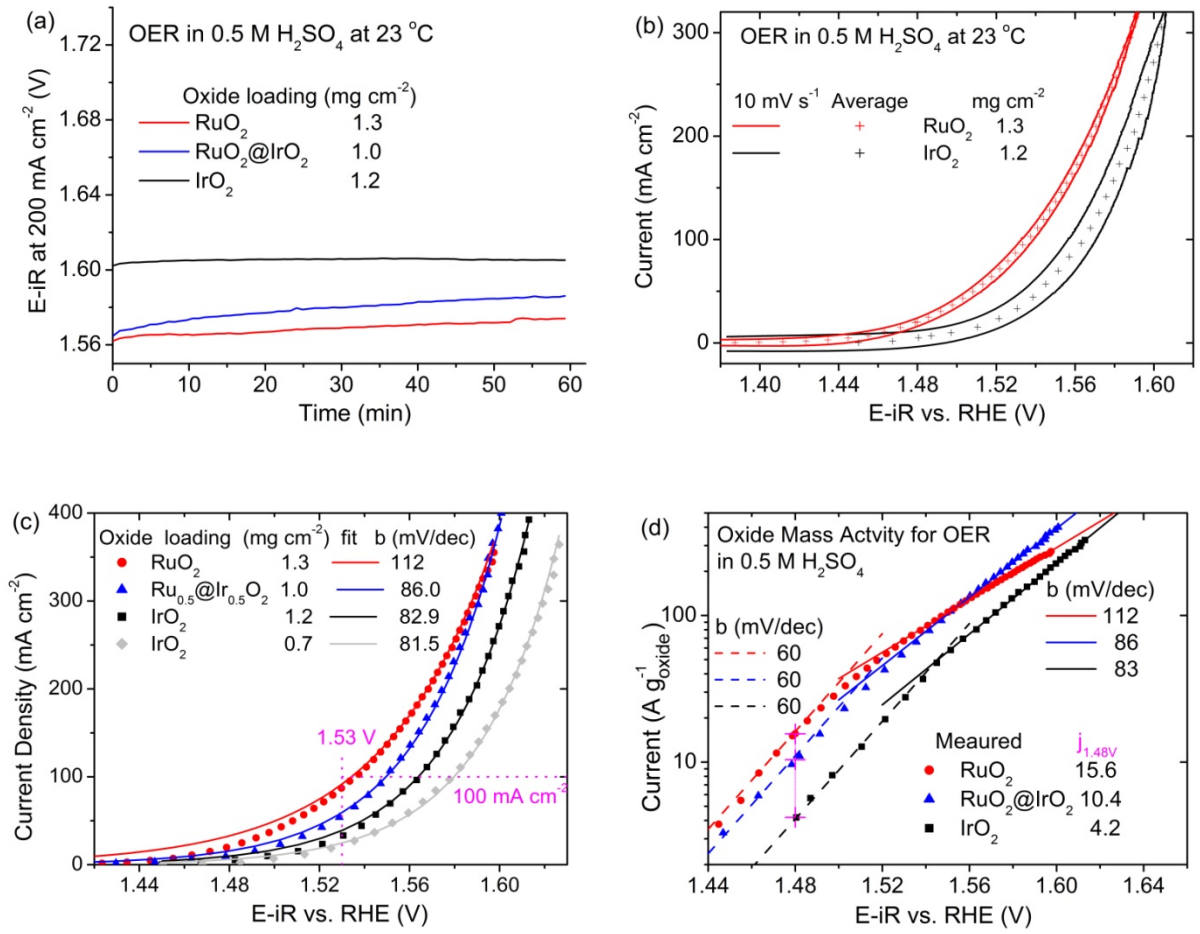

Figure 4. (a) Chronopotentiometry for OER at 200 mA cm^{-2} for three oxide nanocatalysts on Ti gas diffusion electrodes in 0.5 M H_2SO_4 solution. (b) OER currents in positive and negative sweeps (lines) and the averaging currents (+ signs). (c) Steady-state OER polarization curves (symbols) measured after 1 h chronopotentiometry with the best fits (solid lines) using the Butler-Volmer equation with a constant Tafel slope, *b*, which reproduced the data above 1.53 V. (d) Oxide-mass-normalized polarization curves with the Tafel lines and marked mass activities at 1.48 V.

Figure 4c compares the measured polarization curves (symbols) for the RuO_2, IrO_2, and RuO_2@IrO_2 catalysts. The solid lines are the best fits using the Butler-Volmer equation, $j = j_0 e^{2.303(E-1.23)/b}$, where j_0 is the exchange current and b is the Tafel slope. The data at potentials above 1.53 V were well reproduced in all four curves by the fits using a constant Tafel slope. The fitted Tafel slopes were reproduced by samples with different catalysts' loadings, as

illustrated by the two IrO_2 samples. Figure 4d shows the mass-normalized current on logarithmic scale for the three catalysts. While the Tafel slopes are all about 60 mV/dec at low overpotentials, the characteristic high-overpotential Tafel slopes are considerably smaller for RuO_2@IrO_2 (86 mV/dec) and IrO_2 (83 mV/dec) than for RuO_2 (112 mV/dec). At 1.48 V (0.25 V overpotential), the oxide mass activity of ~3 nm RuO_2@IrO_2 (10.4 g^{-1}_{ox}) is 2.5 times of that for the ~2 nm IrO_2 (4.2 A g^{-1}_{ox}), and is 33% lower than ~9 nm RuO_2 (15.6 A g^{-1}_{ox}). To gain insight on reaction mechanism, we show in next section, the analysis of surface-area-normalized polarization curves.

4.4. *OER specific activity and kinetic analysis*

Based on the surface areas determined in Section 4.2, we plot the surface-area-normalized polarization curves in Fig. 5a, representing the OER specific activities for the three oxide catalysts. At 1.48 V, the OER specific activities of the IrO_2 (1.7 μA cm^{-2}_{ox}) and the RuO_2 (16 μA cm^{-2}_{ox}) samples are comparable with the values of 2 and 10 μA cm^{-2}_{ox}, respectively, measured on rotating disk electrodes [23]. Also, the shapes of the curves are in the same trend with the Tafel slopes at high potentials being larger for RuO_2 than for IrO_2 [23]. The RuO_2@IrO_2 (5.5 μA cm^{-2}_{ox}) sample exhibited threefold specific activity and similar Tafel slope as compared with the IrO_2.

Fitting or simulating polarization curves were commonly carried out using equations with the adsorption isotherms of reaction intermediates being derived based on the steady-state principle [54–58]. For the OER, kinetic equations involving *OH and *O as the reaction intermediates were derived with reaction rates and equilibrium constants as the kinetic parameters [55,58]. The results demonstrated a variety of possible Tafel slopes [58] and the ability to simulate measured OER polarization curve for IrO_2 [55]. However, the reaction rate and equilibrium constants for multiple reaction intermediates were not determined from fitting measured polarization curves. To facilitate comparison with DFT calculations, we derived here the OER kinetic equation using activation and adsorption free energies as the kinetic parameters. A simple kinetic model is adapted to minimize the number of parameters, which considers the sequential water dissociation pathway in two major reaction steps and one major adsorbed intermediate, O_{ad}:

$$\tfrac{1}{2}\,H_2O \quad = \tfrac{1}{2}\,O_{ad} + H^+ + e^- \tag{1}$$

$$\tfrac{1}{2}\,H_2O + \tfrac{1}{2}\,O_{ad} = \tfrac{1}{2}\,O_2 + H^+ + e^- \tag{2}$$

Compared to the DFT calculations, the first step here includes the elementary reactions of water dissociation on oxide surface and oxidative deprotonation to *O*H and *O; the second step involves water dissociative adsorption of another O in forming *OOH, deprotonation, and O_2 evolution.

Following the conventions detailed in our previous derivation of the dual-pathway kinetic equation for the HER-HOR [9,56], and the double-trap kinetic equation for the ORR [57], the currents for first and second reactions in the forward (+) and backward (-) directions can be written as

$$j_1 = j_{+1} - j_{-1} = j^* e^{-\Delta G_{+1}/kT}(1-\theta) - j^* e^{-\Delta G_{-1}/kT}\theta \tag{3}$$

$$j_2 = j_{+2} - j_{-2} = j^* e^{-\Delta G_{+2}/kT}\theta - j^* e^{-\Delta G_{-2}/kT}(1-\theta) \tag{4}$$

where j^* = 1000 A cm^{-2} is a fixed reference pre-factor [56], kT = 25.51 meV at 23 °C, θ is the fractional coverage of the reaction intermediate, O_{ad}, and ΔG_i is the activation free energy for the reaction labeled by the subscript i. The activation free energies vary with the overpotential $\eta = E_{RHE} - E^0$, where E^0 is the oxygen reversible potential, as given below:

$$\Delta G_{+1} = \Delta G_1^0 \quad - \alpha_1 e\eta \tag{5}$$

$$\Delta G_{-1} = \Delta G_1^0 - \Delta G_{ad}^0 + (1-\alpha_1)e\eta \tag{6}$$

$$\Delta G_{+2} = \Delta G_2^0 - \Delta G_{ad}^0 - \alpha_2 e\eta \tag{7}$$

$$\Delta G_{-2} = \Delta G_2^0 \quad + (1-\alpha_2)e\eta \tag{8}$$

In which, α is the transfer coefficient, superscript ^{0} means at zero overpotential relative to E^0. Here, we define the standard activation free energies $\Delta G_1^0 \equiv \Delta G_{+1}(\eta = 0)$, $\Delta G_2^0 \equiv \Delta G_{-2}(\eta = 0)$, and the standard adsorption free energy $\Delta G_{ad}^0 \equiv -\ln(\theta^0/(1-\theta^0))$ as the independent

parameters. Figure S1 illustrates the relationship among the activation barriers for the two reactions in two directions, and the three independent free energy parameters.

Based on the steady-state principle, the total kinetic current, j_k, and the coverage of the intermediate, θ, are invariant with time at any potential, so that the net reaction rate of the first reaction that adds O_{ad} on the surface must equal the net reaction rate of the second reaction that removes O_{ad} from the surface. Therefore, we have $j_1 = j_2$ and thus the kinetic equation can be expressed using either j_1 or j_2.

$$j_k = j^* e^{-\Delta G_{+1}/kT}(1-\theta) - j^* e^{-\Delta G_{-1}/kT}\theta = j^* e^{-\Delta G_{+2}/kT}\theta - j^* e^{-\Delta G_{-2}kT}(1-\theta) \qquad (9)$$

Rearranging this steady-state equation gives us the adsorption isotherm expressed as a fractional coverage of the OER intermediate,

$$\theta = \frac{g_{+1} + g_{-2}}{g_{+1} + g_{-1} + g_{+2} + g_{-2}} \qquad (10)$$

where $g_i = e^{-\Delta G_i/kT}$ with ΔG_i given in Eqs. 5-7.

In fitting the measured polarization curves in Fig. 5a using above derived kinetic equation, we allowed the two activation free energies ΔG_1^0 and ΔG_2^0 to vary during fitting with fixed α_1, α_2 and ΔG_{ad}^0 values, and reset the fixed parameters for each run. As shown by the solid lines in Fig. 6a, the entire polarization curves were well reproduced by the best fits. The transfer coefficients need to be $\alpha_1 = \alpha_2 = 0.5$ for the RuO_2 and $\alpha_1 = 0.7$ and $\alpha_2 = 0.3$ for the IrO_2 and RuO_2@IrO_2. Good fits can be obtained with a range of ΔG_{ad}^0 values with adjusted ΔG_1^0 and ΔG_2^0. The uniqueness of the best fits would increase if experimentally determined adsorption isotherms $\theta(E)$ were also available for fitting. We report here the sets of parameters for the three catalysts obtained with ΔG_{ad}^0 at the low end of the range (listed in Fig. 5a).

Using the fitted parameters, we show in Fig. 5b the corresponding adsorption isotherms, $\theta(E)$, and in Fig. 5c the OER free energy diagrams at 0 V (dashed lines) and 0.25 V (dotted lines) overpotentials. The fractional coverage of O_{ad} is closely correlated to the O adsorption free energy. The high ΔG_{ad}^0 for all three oxide surfaces prohibit the formation of O_{ad} phase, and thus,

any OER activity at 1.23 V. At 1.48 V (or 0.25 V overpotential), the fractional coverage of O_{ad} on the RuO_2 surface rises to about 0.5 when its ΔG_{ad} (= ΔG^0_{ad} - 0.25 eV) is lowered to near 0. The ΔG^0_{ad} values are considerably higher for IrO_2 and RuO_2@IrO_2, so the O_{ad} coverage rises more gradually. The rate-limiting steps are identified by the highest barriers. For the IrO_2 and RuO_2@IrO_2, ΔG^0_1 is larger than ΔG^0_2 - ΔG^0_{ad}. Thus, the formation of the O_{ad} phase is the rate-limiting step (black arrows). In contrast, ΔG^0_1 is smaller than ΔG^0_2 - ΔG^0_{ad} for RuO_2, so the reaction rate is limited by the second step (red arrows) involving the O-O bond formation before O_{ad} desorbs from the surface.

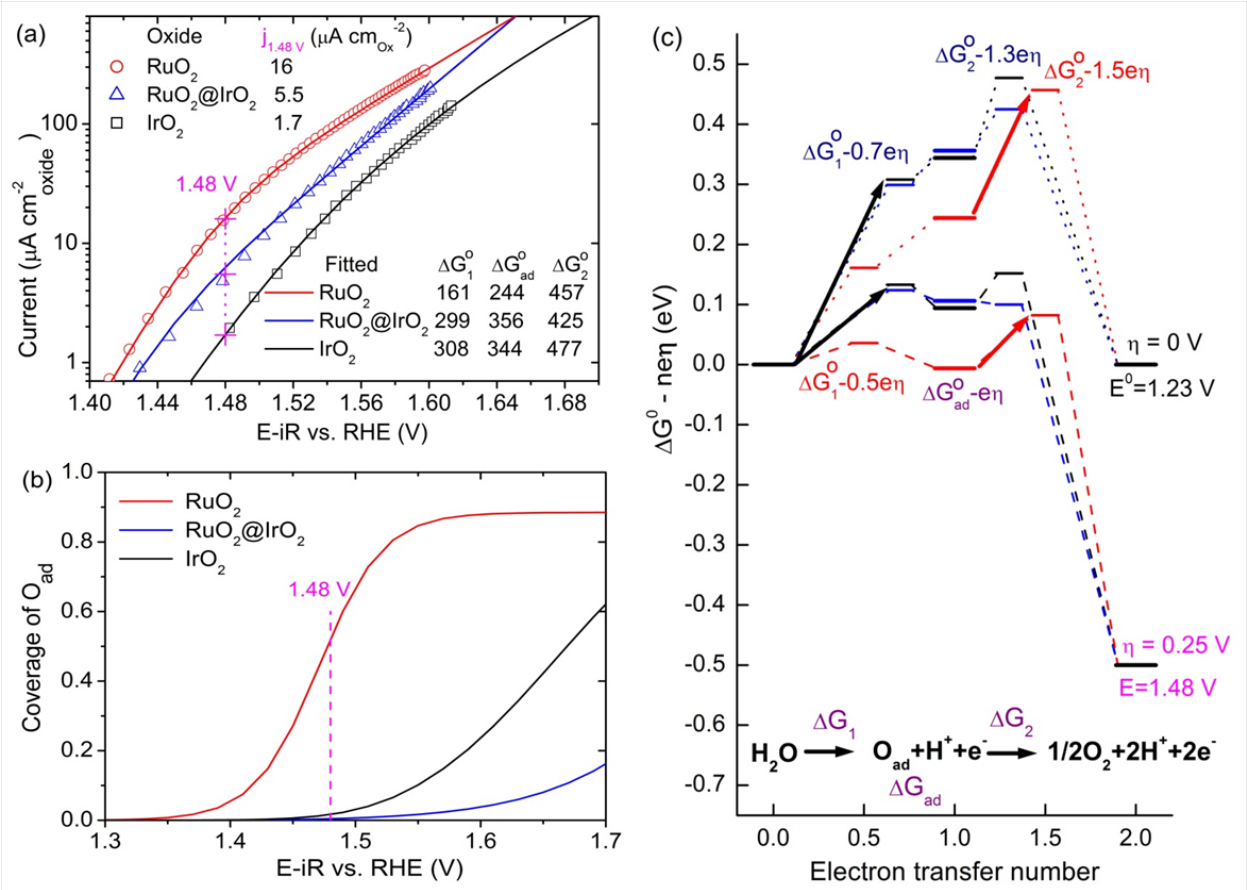

Figure 5. (a) Surface-area-normalized polarization curves (symbols) obtained using the same metal oxide loadings as in Fig. 4a and the best fits (lines) using the sequential OER kinetic equation. The fitted kinetic parameters are the standard free energies given in unit of meV. (b) Adsorption isotherm for the OER intermediate O_{ad} calculated, and (c) OER free energy diagrams at 0 and 0.25 V overpotentials constructed, using the standard free energies listed in (a). Color schemes: RuO_2 (red), RuO_2@IrO_2 (blue), and IrO_2 (black).

5. Discussion

Comparisons of experimental and theoretical results are shown in Fig. 6. For the three oxide catalysts, Fig. 6a shows the experimental ΔG^0_{ad} (zero is defined at the oxygen reversible potential, E = 1.23 V vs. RHE, for $H_2O = 1/2O_2 + 2H^+ + 2e^-$) versus the DFT-calculated ΔG^0_{*O}, which equals $\Delta G_{*O} / 2 - 1.23$ eV, where ΔG_{*O} is the reaction free energy (shown by the thick bars in Fig. 1d) calculated for $2H_2O = O_2 + 4H^+ + 4e^-$ (thus dividing by 2) at E = 0 (1e × 1.23 V = 1.23 eV). A linear relationship is demonstrated for the three oxide catalysts, which supports the use of ΔG^0_{*O} (or ΔG_{*O}) as the descriptor for the OER activities of the oxide catalysts.

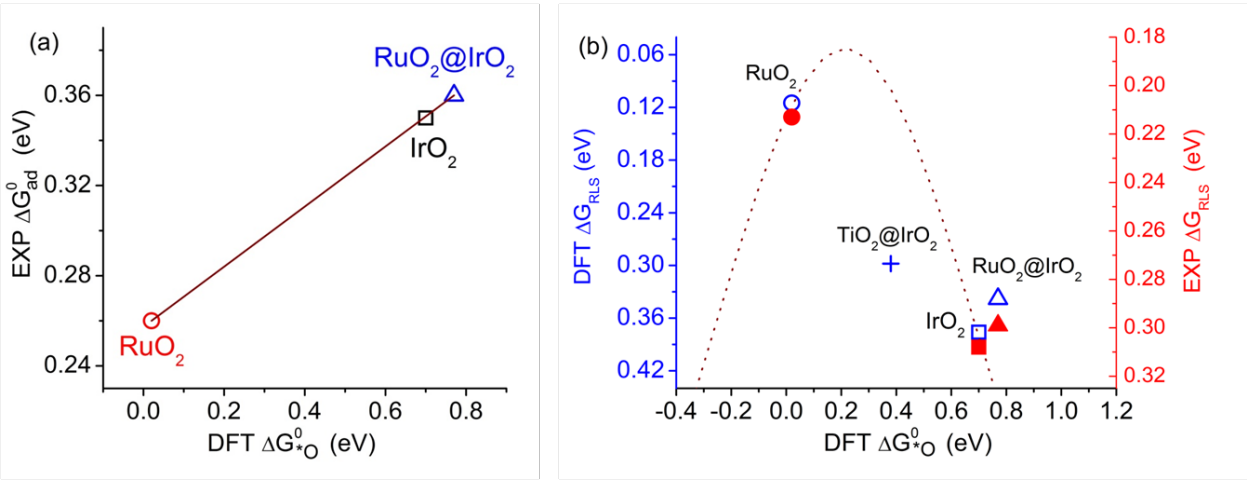

Figure 6. (a) Linear relationship between experimental and theoretical adsorption free energies at oxygen reversible potential (η = 0 V, E = 1.23 V). (b) Comparison of activation barriers for the rate-limiting step obtained from DFT calculations (blue symbols, left axis) and kinetic analyses (red solid symbols, right axis).

In Fig. 6b, we plot the activation barrier for the rate-limiting step (open symbols in blue, left axis) based on DFT-calculated reaction free energies in comparison with the values derived experimentally (solid symbols in red, right axis). The conversion of the DFT barriers for the rate-limiting steps (1.46, 1.83, 1.91, and 1.98 eV discussed in Section 3) involves dividing by 2 (the reaction formula used in kinetic analysis and DFT calculation differ by a factor 2) and subtracting 0.625 eV (a transfer coefficient of 0.5 with a potential shift of 1.23 V). We plot the lower activation barriers upward in Fig. 6b as they represent higher activities. The relative activities of RuO_2, IrO_2 and RuO_2@IrO_2 estimated by the DFT calculations (blue open symbols)

are consistent with the trend determined experimentally (red solid symbols). Based on the rate-limiting step being after and before the formation of *O for RuO_2 and IrO_2, respectively, a volcano curve (dotted line) is drawn, having RuO_2 on the left side of the optimal ΔG^0_{*O} and the IrO_2 on the right side. Both TiO_2@IrO_2 and RuO_2@IrO_2 are on the right side, consistent with their rate-limiting step being the same as that of IrO_2.

Relative to IrO_2, ΔG^0_{*O} increases on the IrO_2 shell with a RuO_2 core and decreases with a TiO_2 core. The effects can be explained by the general trend of core-induced surface contraction and expansion, respectively, since the lattice constants are in the order of RuO_2 < IrO_2 < TiO_2. For the activation barrier of the rate-limiting step along the y-axis, however, the calculated values (blue plus and triangle) are not exactly on the volcano curve. As the experimental result is consistent with the calculated barrier for the RuO_2@IrO_2 core-shell catalyst, we can consider the volcano curve as a main trend, and use the calculated barriers as detailed prediction and guidance in designing and optimizing oxide core-shell nanocatalysts. Interestingly, the activation barrier for the rate-limiting step for the TiO_2@IrO_2 (blue plus in Fig. 6b) was found lower than those for IrO_2 and RuO_2@IrO_2. This can be important for developing advanced OER catalysts for PEM water electrolysis because TiO_2 is stable in acid and Ti is not a precious metal.

6. **Conclusion**

This study shows a feasible synthesis method to prepare active RuO_2 and RuO_2@IrO_2 nanocatalysts for the OER in acids, and elucidates the OER mechanism in acid on most active metal dioxides. Both DFT calculated and experimentally derived free energy diagrams support the reaction mechanism with the O-O bond forming via sequential water dissociative adsorption on a single metal site. To be highly active for the OER, the *O phase needs to be stable enough so that it can be formed at low overpotentials, but also needs to be reactive enough for water dissociation on adsorbed O in forming the O-O bond. From this viewpoint, the formation of the *O phase by oxidative desorption of two protons following water dissociative adsorption is slightly too hard on IrO_2, while the more easily forming *O phase on RuO_2 is slightly too stable, and thus, not reactive enough to facilitate water dissociative adsorption in forming the *OO*H phase. Based on the DFT calculations, the effect of a RuO_2 core on the IrO_2 monolayer shell

slightly reduces the *O adsorption strength, which is not ideal, and TiO_2 is likely a more suitable oxide core than RuO_2. The insight can help developing more active OER catalysts.

Acknowledgments

This research was supported by the U.S. Department of Energy, Office of Basic Energy Science under contract DE-SC0012704 and Office of Energy Efficiency and Renewable Energy under grant DE-FG02-12ER86531. The XRD study at the Advanced Photon Source operated by Argonne National Laboratory was supported by U.S. Department of Energy, Office of Science under Contract No. DE-AC02-06CH11357. The DFT calculations were performed using the computational resources at the Center for Functional Nanomaterials, a user facility at Brookhaven National Laboratory. Z.M. acknowledges financial support from the National Natural Science Foundation of China (21336003) and the Major Basic Research Program of China (2014CB239703).

References

[1] M.B. Gawande, A. Goswami, T. Asefa, H. Guo, A. V Biradar, D. Peng, R. Zboril, R.S. Varma, Core-shell nanoparticles: synthesis and applications in catalysis and electrocatalysis, Chem. Soc. Rev. 44 (2015) 7540–7590. doi:10.1039/C5CS00343A.

[2] J.X. Wang, H. Inada, L. Wu, Y. Zhu, Y. Choi, P. Liu, Oxygen Reduction on Well-Defined Core - Shell Nanocatalysts : Particle Size , Facet , and Pt Shell, J. Am. Chem. Soc. 131 (2009) 17298–17302.

[3] P. Strasser, S. Koh, T. Anniyev, J. Greeley, K. More, C. Yu, Z. Liu, S. Kaya, D. Nordlund, H. Ogasawara, M.F. Toney, A. Nilsson, Lattice-strain control of the activity in dealloyed core–shell fuel cell catalysts, Nat. Chem. 2 (2010) 454–460. doi:10.1038/nchem.623.

[4] Y.-C. Hsieh, Y. Zhang, D. Su, V. Volkov, R. Si, L. Wu, Y. Zhu, W. An, P. Liu, P. He, S. Ye, R.R. Adzic, J.X. Wang, Ordered bilayer ruthenium-platinum core-shell nanoparticles as carbon monoxide-tolerant fuel cell catalysts., Nat. Commun. 4 (2013) 2466. doi:10.1038/ncomms3466.

[5] J.R. Kitchin, J.K. Nørskov, M.A. Barteau, J.G. Chen, Modification of the surface

electronic and chemical properties of Pt(111) by subsurface 3d transition metals, J. Chem. Phys. 120 (2004) 10240–10246. doi:10.1063/1.1737365.

[6] J. Zhang, M.B. Vukmirovic, Y. Xu, M. Mavrikakis, R.R. Adzic, Controlling the catalytic activity of platinum-monolayer electrocatalysts for oxygen reduction with different substrates, Angew. Chemie - Int. Ed. 44 (2005) 2132–2135. doi:10.1002/anie.200462335.

[7] K. Sasaki, H. Naohara, Y. Cai, Y.M. Choi, P. Liu, M.B. Vukmirovic, J.X. Wang, R.R. Adzic, Core-protected platinum monolayer shell high-stability electrocatalysts for fuel-cell cathodes., Angew. Chem. Int. Ed. Engl. 49 (2010) 8602–8607. doi:10.1002/anie.201004287.

[8] J.X. Wang, Y. Zhang, C.B. Capuano, K.E. Ayers, Ultralow charge-transfer resistance with ultralow Pt loading for hydrogen evolution and oxidation using Ru@Pt core-shell nanocatalysts, Sci. Rep. 5 (2015) 12220. doi:10.1038/srep12220.

[9] K. Elbert, J. Hu, Z. Ma, Y. Zhang, G. Chen, W. An, P. Liu, H.S. Isaacs, R.R. Adzic, J.X. Wang, Elucidating Hydrogen Oxidation/Evolution Kinetics in Alkaline and Acid Solutions via Optimizing Pt-Shell Thickness on Ru Core, ACS Catal. 5 (2015) 6764–6772. doi:10.1021/acscatal.5b01670.

[10] P. Liu, A. Logadottir, J.K. Nørskov, Modeling the electro-oxidation of CO and H2/CO on Pt, Ru, PtRu and Pt3Sn, Electrochim. Acta. 48 (2003) 3731–3742. doi:10.1016/S0013-4686(03)00538-3.

[11] P.C.K. Vesborg, T.F. Jaramillo, Addressing the terawatt challenge: scalability in the supply of chemical elements for renewable energy, RSC Adv. 2 (2012) 7933. doi:10.1039/c2ra20839c.

[12] M.K. Debe, S.M. Hendricks, G.D. Vernstrom, M. Meyers, M. Brostrom, M. Stephens, Q. Chan, J. Willey, M. Hamden, C.K. Mittelsteadt, C.B. Capuano, K.E. Ayers, E.B. Anderson, Initial Performance and Durability of Ultra-Low Loaded NSTF Electrodes for PEM Electrolyzers, J. Electrochem. Soc. 159 (2012) K165–K176. doi:10.1149/2.065206jes.

[13] M. Carmo, D.L. Fritz, J. Mergel, D. Stolten, A comprehensive review on PEM water electrolysis, Int. J. Hydrogen Energy. 38 (2013) 4901–4934.

doi:10.1016/j.ijhydene.2013.01.151.

[14] K.E. Ayers, J.N. Renner, N. Danilovic, J.X. Wang, Y. Zhang, R. Maric, H. Yu, Pathways to ultra-low platinum group metal catalyst loading in proton exchange membrane electrolyzers, Catal. Today. 262 (2016) 121–132.

[15] H.N. Nong, L. Gan, E. Willinger, D. Teschner, P. Strasser, IrOx core-shell nanocatalysts for cost- and energy-efficient electrochemical water splitting, Chem. Sci. 5 (2014) 2955–2963. doi:10.1039/c4sc01065e.

[16] C. Angelinetta, S. Trasatti, L.D. Atanososka, R.T. Atanasoski, Surface properties of RuO2 + IrO2 mixed oxide electrodes, J. Electroanal. Chem. 214 (1986) 535–546. doi:10.1016/0022-0728(86)80122-X.

[17] R. Kötz, S. Stucki, Stabilization of RuO2 by IrO2 for anodic oxygen evolution in acid media, Electrochim. Acta. 31 (1986) 1311–1316. doi:10.1016/0013-4686(86)80153-0.

[18] A. Marshall, S. Sunde, M. Tsypkin, R. Tunold, Performance of a PEM water electrolysis cell using IrxRuyTazO2IrxRuyTazO2 electrocatalysts for the oxygen evolution electrode, Int. J. Hydrogen Energy. 32 (2007) 2320–2324. doi:10.1016/j.ijhydene.2007.02.013.

[19] S. Song, H. Zhang, X. Ma, Z. Shao, R.T. Baker, B. Yi, Electrochemical investigation of electrocatalysts for the oxygen evolution reaction in PEM water electrolyzers, Int. J. Hydrogen Energy. 33 (2008) 4955–4961. doi:10.1016/j.ijhydene.2008.06.039.

[20] M.E.G. Lyons, S. Floquet, Mechanism of oxygen reactions at porous oxide electrodes. Part 2--Oxygen evolution at RuO2, IrO2 and Ir(x)Ru(1-x)O2 electrodes in aqueous acid and alkaline solution., Phys. Chem. Chem. Phys. 13 (2011) 5314–5335. doi:10.1039/c0cp02875d.

[21] T. Audichon, E. Mayousse, S. Morisset, C. Morais, C. Comminges, T.W. Napporn, K.B. Kokoh, Electroactivity of RuO2–IrO2 mixed nanocatalysts toward the oxygen evolution reaction in a water electrolyzer supplied by a solar profile, Int. J. Hydrogen Energy. 39 (2014) 16785–16796. doi:10.1016/j.ijhydene.2014.07.170.

[22] S. Siracusano, V. Baglio, A. Di Blasi, N. Briguglio, A. Stassi, R. Ornelas, E. Trifoni, V. Antonucci, A.S. Aricò, Electrochemical characterization of single cell and short stack PEM electrolyzers based on a nanosized IrO2 anode electrocatalyst, Int. J. Hydrogen

Energy. 35 (2010) 5558–5568. doi:10.1016/j.ijhydene.2010.03.102.

[23] Y. Lee, J. Suntivich, K.J. May, E.E. Perry, Y. Shao-horn, Synthesis and Activities of Rutile IrO 2 and RuO 2 Nanoparticles for Oxygen Evolution in Acid and Alkaline Solutions, J. Phys. Chem. Lett. 3 (2012) 399–404.

[24] S. Cherevko, S. Geiger, O. Kasian, N. Hulyk, J.-P. Gtote, A. Savan, B.R. Shrestha, S. Merzlikin, B. Breitbach, A. Luwig, K.J.J. Mayrhofer, Oxygen and hydrogen evolution reactions on Ru, RuO2, Ir, and IrO2 thin film electrodes in acidic and alkaline electrolytes: A comparative study on activity and stability, Catal. Today. 262 (2016) 170–180. doi:10.1016/j.cattod.2015.08.014.

[25] N. Danilovic, R. Subbaraman, K.C. Chang, S.H. Chang, Y. Kang, J. Snyder, A.P. Paulikas, D. Strmcnik, Y.T. Kim, D. Myers, V.R. Stamenkovic, N.M. Markovic, Using Surface Segregation To Design Stable Ru-Ir Oxides for the Oxygen Evolution Reaction in Acidic Environments, Angew. Chemie. 126 (2014) 14240–14245. doi:10.1002/anie.201406455.

[26] T. Reier, H.N. Nong, D. Teschner, R. Schlögl, P. Strasser, Electrocatalytic Oxygen Evolution Reaction in Acidic Environments - Reaction Mechanisms and Catalysts, Adv. Energy Mater. (2016) 1601275. doi:10.1002/aenm.201601275.

[27] J.O. Bockris, Kinetics of Activation Controlled Consecutive Electrochemical Reactions: Anodic Evolution of Oxygen, J. Chem. Phys. 24 (1956) 817. doi:10.1063/1.1742616.

[28] Y. Matsumoto, E. Sato, Electrocatalytic properties of transition metal oxides for oxygen evolution reaction, Mater. Chem. Phys. 14 (1986) 397–426. doi:10.1016/0254-0584(86)90045-3.

[29] H. Dau, C. Limberg, T. Reier, M. Risch, S. Roggan, P. Strasser, The Mechanism of Water Oxidation: From Electrolysis via Homogeneous to Biological Catalysis, ChemCatChem. 2 (2010) 724–761. doi:10.1002/cctc.201000126.

[30] E. Fabbri, A. Habereder, K. Waltar, R. Kötz, T.J. Schmidt, R. Kotz, T.J. Schmidt, Developments and perspectives of oxide-based catalysts for the oxygen evolution reaction, Catal. Sci. Technol. 4 (2014) 3800–3821. doi:10.1039/C4CY00669K.

[31] E. Antolini, Iridium as catalyst and cocatalyst for oxygen evolution/reduction in acidic

polymer electrolyte membrane electrolyzers and fuel cells, ACS Catal. 4 (2014) 1426–1440. doi:10.1021/cs4011875.

[32] J. Rossmeisl, A. Logadottir, J.K. Nørskov, Electrolysis of water on (oxidized) metal surfaces, Chem. Phys. 319 (2005) 178–184. doi:10.1016/j.chemphys.2005.05.038.

[33] J. Rossmeisl, Z.-W. Qu, H. Zhu, G.-J. Kroes, J.K. Nørskov, Electrolysis of water on oxide surfaces, J. Electroanal. Chem. 607 (2007) 83–89. doi:10.1016/j.jelechem.2006.11.008.

[34] M.T.M. Koper, Thermodynamic theory of multi-electron transfer reactions: Implications for electrocatalysis, J. Electroanal. Chem. 660 (2011) 254–260. doi:10.1016/j.jelechem.2010.10.004.

[35] I.C. Man, H.-Y. Su, F. Calle-Vallejo, H.A. Hansen, J.I. Martínez, N.G. Inoglu, J. Kitchin, T.F. Jaramillo, J.K. Nørskov, J. Rossmeisl, Universality in Oxygen Evolution Electrocatalysis on Oxide Surfaces, ChemCatChem. 3 (2011) 1159–1165. doi:10.1002/cctc.201000397.

[36] F. Calle-Vallejo, J.I. Martínez, J.M. García-Lastra, E. Abad, M.T.M. Koper, Oxygen reduction and evolution at single-metal active sites: Comparison between functionalized graphitic materials and protoporphyrins, Surf. Sci. 607 (2013) 47–53. doi:10.1016/j.susc.2012.08.005.

[37] Y.H. Fang, Z.P. Liu, Mechanism and tafel lines of electro-oxidation of water to oxygen on RuO2(110), J. Am. Chem. Soc. 132 (2010) 18214–18222. doi:10.1021/ja1069272.

[38] M.D. Segall, P.J.D. Lindan, M.J. Probert, C.J. Pickard, P.J. Hasnip, S.J. Clark, M.C. Payne, First-principles simulation: ideas, illustrations and the CASTEP code, J. Phys. Condens. Matter. 14 (2002) 2717–2744. doi:10.1088/0953-8984/14/11/301.

[39] S.J. Clark, M.D. Segall, C.J. Pickard, P.J. Hasnip, M.I.J. Probert, K. Refson, M.C. Payne, First principles methods using CASTEP, Zeitschrift Fur Krist. 220 (2005) 567–570. doi:10.1524/zkri.220.5.567.65075.

[40] J. Perdew, K. Burke, Y. Wang, Generalized gradient approximation for the exchange-correlation hole of a many-electron system, Phys. Rev. B. 54 (1996) 16533–16539. doi:10.1103/PhysRevB.54.16533.

[41] J.P. Perdew, K. Burke, M. Ernzerhof, Generalized Gradient Approximation Made Simple,

Phys. Rev. Lett. 77 (1996) 3865–3868. doi:10.1103/PhysRevLett.77.3865.

[42] H.J. Monkhorst, J.D. Pack, Special points for Brillouin-zone integrations, Phys. Rev. B. 13 (1976) 5188–5192. doi:10.1103/PhysRevB.13.5188.

[43] A.A. Bolzan, C. Fong, B.J. Kennedy, C.J. Howard, A . A . Bolzan , C . Fong , B . J . Kennedy and C . J . Howard, Acta Crystallogr. Sect. B. 53 (1997) 373–380.

[44] W. An, P. Liu, Size and Shape Effects of Pd@Pt Core−Shell Nanoparticles: Unique Role of Surface Contraction and Local Structural Flexibility, J. Phys. Chem. C. 117 (2013) 16144–16149. doi:10.1021/jp4057785.

[45] W. An, P. Liu, Rationalization of Au Concentration and Distribution in AuNi@Pt Core-Shell Nanoparticles for Oxygen Reduction Reaction, ACS Catal. 5 (2015) 6328–6336. doi:10.1021/acscatal.5b01656.

[46] C. Felix, T. Maiyalagan, S. Pasupathi, B. Bladergroen, V. Linkov, Synthesis and Optimisation of IrO2 Electrocatalysts by Adams Fusion Method for Solid Polymer Electrolyte Electrolysers, Micro Nanosyst. 4 (2012) 186–191. doi:10.2174/1876402911204030186.

[47] S. Siracusano, N. Van Dijk, E. Payne-Johnson, V. Baglio, A.S. Aricò, Nanosized IrOx and IrRuOx electrocatalysts for the O2 evolution reaction in PEM water electrolysers, Appl. Catal. B Environ. 164 (2015) 488–495. doi:10.1016/j.apcatb.2014.09.005.

[48] K.A. Stoerzinger, L. Qiao, M.D. Biegalski, Y. Shao-Horn, Orientation-Dependent Oxygen Evolution Activities of Rutile IrO 2 and RuO 2, J. Phys. Chem. Lett. 5 (2014) 1636–1641. doi:10.1021/jz500610u.

[49] F.L.S. Purgato, L.A. Montoro, J. Ribeiro, K.B. Kokoh, P. Olivi, The Effect of Heat Treatment on the Preparation of Pt-RuO2/C Electrocatalysts, Electrocatalysis. 1 (2010) 122–128. doi:10.1007/s12678-010-0019-9.

[50] Z.W. Ulissi, A.R. Singh, C. Tsai, J.K. Nørskov, Automated Discovery and Construction of Surface Pourbaix Diagrams using Machine Learning, J. Phys. Chem. Lett. 7 (2016) 3931–3935. doi:10.1021/acs.jpclett.6b01254.

[51] K. Doblhofer, M. Metikos, Z. Ogumi, H. Gerischer, Electrochemical Oxidation and Reduction, Ber. Bunsengess. Phys. Chem. 82 (1978) 1046–1050.

doi:10.1002/ijch.198500093.

[52] E. Watanabe, J. Rossmeisl, M.E. Björketun, H. Ushiyama, K. Yamashita, Atomic-Scale Analysis of the RuO2/Water Interface under Electrochemical Conditions, J. Phys. Chem. C. 120 (2016) 8096–8103. doi:10.1021/acs.jpcc.5b12448.

[53] F.. Mattos-Costa, P. de Lima-Neto, S. a. . Machado, L.. Avaca, Characterisation of surfaces modified by sol-gel derived RuxIr1−xO2 coatings for oxygen evolution in acid medium, Electrochim. Acta. 44 (1998) 1515–1523. doi:10.1016/S0013-4686(98)00275-8.

[54] M.R. Gennero De Chialvo, A.C. Chialvo, Hydrogen diffusion effects on the kinetics of the hydrogen electrode reaction. Part I. Theoretical aspects, Phys. Chem. Chem. Phys. 6 (2004) 4009–4017. doi:10.1039/b402695k.

[55] J.M. Hu, J.Q. Zhang, C.N. Cao, Oxygen evolution reaction on IrO2-based DSA?? type electrodes: Kinetics analysis of Tafel lines and EIS, Int. J. Hydrogen Energy. 29 (2004) 791–797. doi:10.1016/j.ijhydene.2003.09.007.

[56] J.X. Wang, T.E. Springer, P. Liu, M. Shao, R.R. Adzic, Hydrogen Oxidation Reaction on Pt in Acidic Media: Adsorption Isotherm and Activation Free Energies, J. Phys. Chem. C. 111 (2007) 12425–12433. doi:10.1021/jp073400i.

[57] J.X. Wang, J. Zhang, R.R. Adzic, Double-trap kinetic equation for the oxygen reduction reaction on Pt(111) in acidic media., J. Phys. Chem. A. 111 (2007) 12702–10. doi:10.1021/jp076104e.

[58] A.T. Marshall, L. Vaisson-Béthune, Avoid the quasi-equilibrium assumption when evaluating the electrocatalytic oxygen evolution reaction mechanism by Tafel slope analysis, Electrochem. Commun. 61 (2015) 23–26. doi:10.1016/j.elecom.2015.09.019.